

Electronic Supplementary Information

Highly Efficient CO₂ Electrochemical Reduction on Dual Metal (Co-Ni)-Nitrogen Sites

Jianping Chen¹, Md Robayet Ahasan², Jin-Su Oh³, Jake A. Tan⁴, Stephen Hennessey⁵, Mahmoud M. Kaid⁵, Hani M. El-Kaderi⁵, Lin Zhou^{3,6}, Ka Un Lao⁵, Ruigang Wang², and Wei-Ning Wang^{1}*

¹Department of Mechanical and Nuclear Engineering, Virginia Commonwealth University,
Richmond, VA 23284, USA

²Department of Metallurgical and Materials Engineering, The University of Alabama,
Tuscaloosa, AL 35487, USA

³Division of Materials Sciences and Engineering, Ames National Laboratory, Ames, IA 50011,
USA

⁴Department of Chemistry, Gottwald Center for the Sciences, University of Richmond,
Richmond, VA 23173, USA

⁵Department of Chemistry, Virginia Commonwealth University, Richmond, VA 23284, USA

⁶Department of Materials Science and Engineering, Iowa State University, Ames, IA 50011,
USA

*Corresponding author: wnwang@vcu.edu

CONTENTS

- S1. Experimental Methods
- S2. Fourier Transform Infrared Spectroscopy
- S3. Powder X-Ray Diffraction
- S4. Scanning Electron Microscopy
- S5. Thermogravimetric Analysis
- S6. Inductive Coupled Plasma Optical Emission Spectroscopy
- S7. Supplementary XPS Spectra
- S8. Raman Spectroscopy
- S9. Diffuse Reflectance Infrared Fourier Transform Spectroscopy
- S10. Temperature-Programmed Analyses
- S11. Additional Electron Microscopy
- S12. Linear Sweep Voltammetry
- S13. ^1H Nuclear Magnetic Resonance
- S14. Electrochemically Active Surface Area (ECSA) and Nyquist Plots
- S15. Catalytic Performance Table
- S16. Density Functional Theory (DFT) Calculations

S1. Experimental Methods

Materials. Cobalt(II) nitrate hexahydrate ($\text{Co}(\text{NO}_3)_2 \cdot 6\text{H}_2\text{O}$, 99.999%), zinc nitrate hexahydrate ($\text{Zn}(\text{NO}_3)_2 \cdot 6\text{H}_2\text{O}$, 99.999%), nickel(II) nitrate hexahydrate ($\text{Ni}(\text{NO}_3)_2 \cdot 6\text{H}_2\text{O}$, 99.999%), 2-methylimidazole ($\text{C}_4\text{H}_6\text{N}_2$, 99%, Sigma-Aldrich), potassium bicarbonate (KHCO_3 , 99.95%), Chelex[®] 100 resin (Na form), potassium chloride (KCl, 99%), dimethyl sulfoxide ($(\text{CH}_3)_2\text{SO}$, 99.9%), hexane ($\text{CH}_3(\text{CH}_2)_4\text{CH}_3$, 99%), Nafion[™] 117 perfluorinated resin solution (5 wt% in a mixture of lower aliphatic alcohols and water) were purchased from Sigma-Aldrich. Methanol (CH_3OH , 99.9%), ethanol ($\text{C}_2\text{H}_5\text{OH}$, 99.5%), hydrochloric acid (HCl, 36.5 to 38.0%), and sodium hydroxide solution (NaOH, 10 N), were purchased from Fisher Chemical. Carbon cloth (AvCarb 1071 HCB, 99.5%) and FAS-50 membrane (Fumasep) were purchased from the Fuel Cell Store. Deuterium oxide (D_2O , 99.8%) was purchased from Thermo Scientific Chemical. Nitrogen (N_2 , 99.995%) and carbon dioxide (CO_2 , 99.995%) were purchased from Linde Gas. Reagent-grade water (Millipore Type 1, 18.2 $\text{M}\Omega \cdot \text{cm}$) was used as the source of ultrapure water for all applications described below. The above materials were used as received; any chemicals or materials requiring additional preparation are described in their subsections below.

Discussion on pyrolysis-induced Formation of SACs, DASCs, and NPs. Taking ZIF-8 as an example, reticulation of 2-methylimidazole (mIM) with Zn^{2+} leads to the formation of ZIF-8 (see experimental section).¹ The reaction mechanism consists of three steps: coordination, deprotonation, and oligomerization (**Figure S1**). We obtained isostructural M-ZIF-8 ($\text{M}=\text{Co}^{2+}$, Ni^{2+}) with an identical structure to Zn-ZIF-8 by exchanging Zn^{2+} with other cations. The absence of broad N-H stretching band and the presence of metal-nitrogen stretching region in FT-IR spectra (**Figure S2**) prove the formation of M-ZIF-8.² Powder X-ray diffraction (PXRD) patterns (**Figure S3**) indicate that all M-ZIF-8 samples exhibited the characteristics of the predicted powder

diffraction pattern based on the reported crystallographic data (CCDC-602542), implying that all M-ZIF-8 samples were iso-reticular to ZIF-8. Scanning electron microscopy reveals that all M-ZIF-8 crystals (**Figure S4**) had the same rhombic dodecahedral shapes with an average size of 100 nm, suggesting the crystallinity and morphology of the crystals were retained while exchanging the metals residing in the framework.

Preparation of Electrolyte. A solution of 0.1 M KHCO_3 , pH 6.7, saturated with CO_2 was prepared by bubbling CO_2 through the solution for 30 minutes. To ensure the absence of trace metal ion impurities, all electrolyte solutions were prepared using reagent grade water and purified by stirring the electrolyte in regenerated Chelex[®] resin (50 g Chelex[®] per 1 L of 0.1 M electrolyte) for at least 24 hours and stored in glass containers before use.^{3, 4} The Chelex[®] 100 Resin was regenerated according to previous reports with minor modifications.⁵ The as-received Chelex[®] material was stirred in 1 M HCl for 12 hours, then rinsed with 5 L of reagent grade water. The material was subsequently placed in 1 M NaOH at 60 °C with constant stirring for 24 hours. The regenerated Chelex[®] was then rinsed with 8 L of reagent grade water until the pH of the filtrate was below 10.8.

Preparation of Working Electrode. Carbon cloth was cut into $1 \times 3.3 \text{ cm}^2$ pieces with ceramic scissors, treated with 6 M HCl for 12 hours to remove trace metal impurities, and then rinsed extensively with reagent grade water before being air-dried and coated with the target catalyst. To prepare the catalyst ink, 10 mg of the target catalyst was suspended in a mixture solution of 300 μL of ethanol and 100 μL of reagent water. Next, 100 μL of Nafion[™] 117 solution was added, followed by ultrasonication for 2 hours and further ultrasonicated for 30 seconds between the preparation of electrode sets and discarded after the preparation of four sets of three electrodes. The drop-casting technique was selected for electrode preparation to ensure a

controlled loading of the catalysts from the prepared inks.⁶ Typically, 10 μL of the so-prepared ink was drop-casted onto the carbon cloth electrode, yielding a catalyst loading of 0.25 mg cm^{-2} . The effective electrode area in all cases was 1 cm^2 .

Electrochemistry Setup. The electrocatalytic experiments were conducted using an electrochemical analyzer (CHI 660D, CH Instruments), an Ag/AgCl aqueous reference electrode (CHI 111, CH Instruments), and a Pt counter electrode (CHI 115, CH Instruments). Ag/AgCl reference electrodes were stored in 1 M KCl when not in use and were periodically checked against pristine reference electrodes to ensure that potential drift did not occur. All electrochemical measurements were controlled relative to the Ag/AgCl reference electrode with iR compensation and then converted to the reversible hydrogen electrode (RHE) scale according to $E_{RHE} = E_{Ag/AgCl} + 0.235 \text{ V} + 0.0591 \times \text{pH}$. All experiments were performed at ambient temperature ($21 \pm 1 \text{ }^\circ\text{C}$) in a custom-made airtight H-cell with 50 mL catholyte and 50 mL anolyte separated by an FAS-50 anion exchange membrane (AEM). When used as received, the FAS-50 membrane was in bromide form with limited bicarbonate ion exchange capability. To convert the membrane to bicarbonate form, the FAS-50 membranes were pretreated with 0.3 M NaOH solution for 12 hours and then with 0.1 M KHCO_3 solution for 48 hours where they were stored. Prior to each experiment, the H-cell was immersed in piranha solution, which was prepared using a 4:1 v/v ratio of sulfuric acid to hydrogen peroxide, for an hour without additional heating to remove trace organic and metallic residues. The H-cell was then further cleaned by thorough rinsing in reagent grade water and drying in an oven at 120 $^\circ\text{C}$ for an hour.

Product Distribution Analysis. The identification and quantification of all gas-phase products were performed by GC. The outflow of the cathode compartment was injected into the GC a minute prior to the end of the chronoamperometry test by an automatic gas sampling valve.

Two Agilent HP-PLOT Q PT columns and a Molesieve column connected in series were used for effluent separation, while detection was achieved with a thermal conductivity detector (TCD) and flame ionization detector (FID) equipped with the nickel catalyst. The peak position and quantity of the catalytic reduction gas were calibrated with a custom-order gas standard (Linde Gas).

One-dimensional ^1H nuclear magnetic resonance (NMR) spectra measured using a Bruker NanoBay AVANCE III 400 MHz NMR spectrometer were used to determine the peak position of liquid-phase products. To prepare the sample for ^1H NMR analysis, 60 μL of D_2O , 25 μL of 4 mM DMSO, and 515 μL of investigated solution were mixed into the NMR tube (New Era NEUL57). The water pre-saturation method was applied to adjust the intensity of the water signal with a 10% D_2O and 90% H_2O ratio.⁷ The automatic shim program in the ICON-NMR software was applied for shimming of the samples. ^1H NMR spectra were recorded with DMSO as a reference, which position was set to 2.71 ppm, $d_1 = 2$ s, and 32 scans.

All catalytic reduction experiments in this study are presented in terms of Faradaic efficiency (FE). The FE of the products was determined by the following calculation:

$$FE_{product} = \frac{Q_{product}}{Q_{total}} \cdot 100 \quad (\text{S1})$$

$$Q_{product} = n_{product} \cdot z_e^- \cdot F \quad (\text{S2})$$

$$n_{product, GC} = \frac{x_{product, GC} \cdot V_{injected}}{V_{m, 25^\circ\text{C}, 1\text{ bar}}} \quad (\text{S3})$$

$$n_{product, NMR} = x_{product, NMR} \cdot V_{electrolyte} \cdot f_{dilution} \quad (\text{S4})$$

$$Q_{total} = \int_{t_0 + t_{res}}^{t_0} I \cdot dt \quad (S5)$$

where $FE_{product}$ (%) is Faradaic efficiency, or product selectivity, for a given CO₂ ECR product (e.g., CO, CH₄), $Q_{product}$ (C) refers to the charge associated with a specific product, Q_{total} (C) is the total charge at a given potential, $n_{product}$ (mol) is the number of moles for a specific product, z_e^- denotes the number of electrons exchanged per mole of product, F ($96485 \text{ C} \cdot \text{mol}^{-1}$) is the Faraday constant, $n_{product,GC}$ (mol) is the number of moles for a gas-phase product, $x_{product,GC}$ (ppm) is the mole fraction of a gas-phase product as determined by GC analysis, $V_{injected}$ (in our case 0.5 mL) is the volume of gas injected into the GC gas sampling loop, $V_{m, 25^\circ\text{C}, 1 \text{ bar}}$ ($24.47 \times 10^3 \text{ mL} \cdot \text{mol}^{-1}$) is the molar volume of a gas at standard ambient pressure and temperature, $n_{product,NMR}$ (mol) is the number of moles for a liquid-phase product, $x_{product,NMR}$ (mol mL^{-1}), $V_{electrolyte}$ (mL) is the volume of the catholyte, $f_{dilution}$ refers to the dilution factor applicable in cases where the electrolyte was diluted before NMR analysis, t_0 (s) is the time signature corresponding to sample injection, t_{res} (s) is the resolved time related to the injection, which is determined by the volume of the gas sampling loop and CO₂ flow rate, I (A) is the recorded current during the chronoamperometry test.

Methods of Determining ECSA. To measure the Electrochemically Active Surface Area (ECSA) of electrocatalytic materials, double-layer capacitance at the electrode-electrolyte interface is evaluated using cyclic voltammetry (CV), specifically in a potential range free of Faradaic reactions. This region's charging current, indicative of the electrochemical double layer, is proportional to the scan rate, with its slope representing the double-layer capacitance. By comparing this capacitance to that of a known reference surface, ECSA is calculated by $ECSA = C_{DL}/C_{REF}$, reflecting the catalyst's surface area available for electrochemical reactions.^{8,9}

Methods of Calculating TOF. TOF values are reported as a function of overpotential (Figure 5E) using current density along with other necessary parameters according to the following equation:¹⁰

$$TOF = j \times N_A / (F \times n \times \Gamma) \quad (S6)$$

where j , N_A , F , n , Γ represent current density, the Avogadro constant, the Faraday constant, the number of electrons transferred to generate one molecule of the product, and the surface concentration or the exact number of active sites catalyzing the reaction (m^{-2}), respectively.

Characterization Instruments. HAADF-STEM images were collected with a Thermo Fisher (FEI) Titan Themis equipped with a probe-forming aberration corrector operated at 200 kV to achieve a nominal image resolution of 0.08 nm. Transmission electron microscopy (TEM) images were taken on a Tecnai F20 transmission electron microscope operating at an acceleration voltage of 200 kV. All reported electron microscopy images were raw images. X-ray photoelectron spectroscopy (XPS) analysis was carried out with a PHI VersaProbe III X-ray photoelectron spectrometer with Al K α as the excitation source. Charge correction of all spectra was performed by adjusting the adventitious carbon signal of aliphatic compounds (C-C) to 284.8 eV. CasaXPS software (v2.3.25) was used to perform all signal processing and deconvolution. Thermogravimetric analysis (TGA) was acquired in platinum pans under N₂ flow at a heating rate of 6 °C min⁻¹, using a TA Instruments TGA 5500. The bulk composition of Zn, Ni, and Co in the prepared catalyst samples was revealed using inductively coupled plasma optical emission spectroscopy (Agilent 5110 ICP-OES). The samples were run in KED (kinetic energy discrimination) mode, with the in-line aspiration of a multi-element internal standard. The BET surface areas were measured by the nitrogen adsorption-desorption method on a surface area and

porosity analyser (Quantachrome Autosorb iQ). Before measurements, the samples were degassed at 150 °C for 10 h under vacuum. The X-ray diffraction (XRD) patterns were recorded on a Rigaku TTR-III theta-theta rotating anode X-ray diffractometer using Cu K α radiation (45 kV and 40 mA) with a step size of 0.013°. Raman spectra were collected with a Horiba LabRAM HR Evolution spectrometer equipped with an integral microscope. DRIFTS experiments were carried out with samples in a diffuse reflectance reaction chamber (Harrick Scientific) equipped with ZnSe windows, mounted in a Praying Mantis diffuse reflection accessory (Harrick Scientific), and coupled to a Thermo Scientific Nicolet iS50 FTIR spectrometer with a liquid-nitrogen-cooled HgCdTe (MCT-A) detector. Hydrogen temperature-programmed reduction (H₂-TPR) and carbon monoxide temperature-programmed desorption (CO-TPD) measurements were conducted on a Micromeritics Autochem II 2920 with a thermal conductivity detector (TCD).

HAADF imaging. Atomic number and sample thickness affect the contrast in HAADF imaging of Co (and Ni) on nitrogenated amorphous carbon based on the equation $Z_{Co}^2/(Z_C^2 \cdot N_C)$. The number of C atoms along the electron beam direction is denoted as N_C . Hence, even if a single Co atom is situated atop a column containing 405 carbon atoms, the image contrast would still be greater than 5%, making it detectable in digital HAADF images.¹¹ The samples were investigated by an aberration-corrected transmission electron microscope (Titan Cube, Thermo Fisher Scientific Ltd.) at 200 kV. A high-angle annular dark-field (HAADF) detector was used for dark-field imaging in STEM mode with a convergent semi-angle and a collection semi-angle of 18 mrad and 74-200 mrad, respectively. A probe current of 25 pA with a dwelling time of 6 μ s at a resolution of 1024 \times 1024 was used.

H₂-TPR and CO-TPD. Hydrogen temperature-programmed reduction (H₂-TPR) experiment began with the installation of a powder sample weighing between 85 and 90 mg

sandwiched by two pieces of quartz wool into quartz U-tube. The temperature of the sample increased linearly from 30 °C to 900 °C at a constant ramping rate of 10°C/min with 10 vol% H₂ - 90 vol% Ar gas mixture flow (flow rate: 50 mL/min). The quantity of H₂ absorbed (consumed) was precisely monitored using a thermal conductivity detector (TCD).

Similarly, carbon monoxide temperature-programmed desorption (CO-TPD) was initiated with a pre-He-purging step at 600 °C for surface cleaning. The helium purging involved heating the sample (~50 mg) from room temperature to 400 °C with a ramping of 10 °C per minute under a He stream at 50 mL/min. After cooled to room temperature, 10 vol% CO - 90 vol% He gas mixture was passed through the sample at a flow rate of 50 mL/min for 60 minutes for CO chemisorption. Subsequently, CO-TPD was performed by heating the sample from 30 °C to 800 °C at a linear ramping rate of 10°C/min under He stream. The gas flow/emission is analyzed by a thermal conductivity detector.¹² The gas flow/emission is analyzed 223 by a thermo conductivity detector. The measurement protocol was analogous to those reported in our previous study.

ICP-OES. ICP-OES was used to analyze the proportion of Co and Ni and the average metal weight percent in the pristine and carbonized Co-Ni-ZIF-8, where 10 mg of each sample was digested in aqua regia overnight and prepared into 5% nitric acid matrices. Subsequently, the samples were centrifuged and introduced into the ICP-OES instrument, where the elements of interest were excited by plasma and their emissions were quantified using spectroscopic analysis. Calibration curves were generated using standard solutions of known concentrations to accurately determine the Co and Ni concentrations in the catalyst samples.

DRIFTS. In a typical experiment, the sample cup was filled with catalyst powder. All gases flowed downward through the catalyst bed. For fresh catalysts, a pretreatment at 150 °C with He was conducted for 30 min. The background spectrum was recorded after the temperature

dropped to 25 °C. CO₂ adsorption was conducted by switching the flowing gas to 15 ml min⁻¹ of 10% CO₂/He. The CO₂ adsorption spectra were continuously recorded as a function of time to investigate the CO₂ adsorption behaviour on the catalysts.

S2. Fourier Transform Infrared Spectroscopy

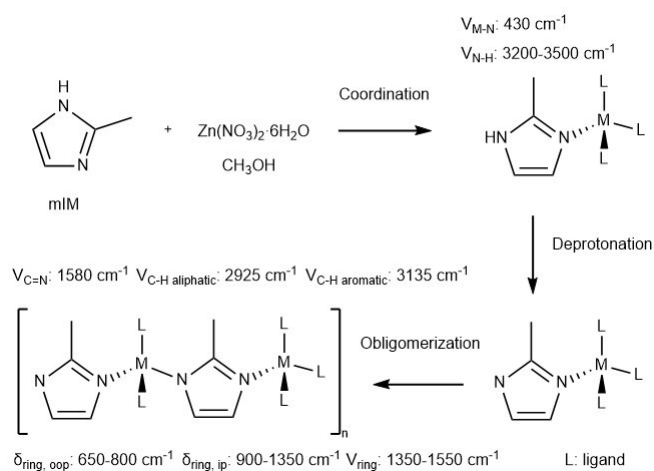


Figure S1. Formation mechanism of ZIF-8 along with the characteristic FTIR band signatures.

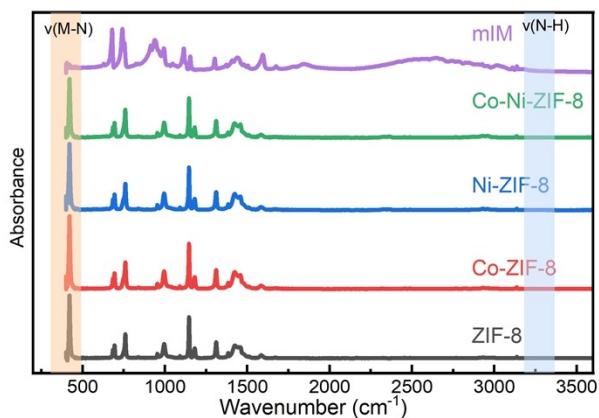


Figure S2. Comparison of FT-IR spectra of the 2-methylimidazole linker, Co-ZIF-8, Ni-ZIF-8, and Co-Ni-ZIF-8. Deprotonation of the 2-methylimidazole linker and the coordination of metal ions are evidenced by the stretching region of $\nu(\text{M-N})$ and $\nu(\text{N-H})$ in FT-IR spectra.

S3. Powder X-Ray Diffraction

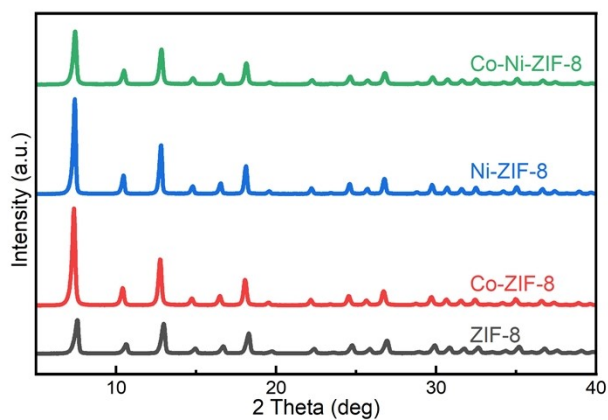


Figure S3. X-ray diffractograms of pristine ZIF-8 and metal doped ZIF-8 (Co-ZIF-8, Ni-ZIF-8, and Co-Ni-ZIF-8).

S4. Scanning Electron Microscopy

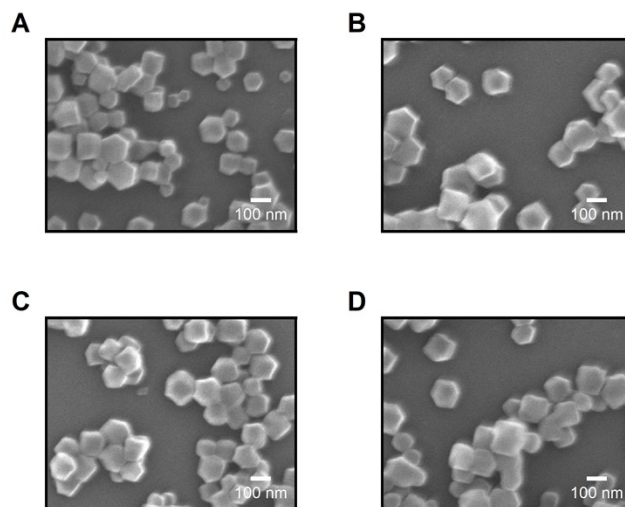


Figure S4. (A-B) Scanning electron microscopy (SEM) images of pristine and metal-doped ZIF-8 samples. (A) ZIF-8. (B) Co-ZIF-8. (C) Ni-ZIF-8. (D) Co-Ni-ZIF-8. Scale bar, 100 nm.

S5. Thermogravimetric Analysis

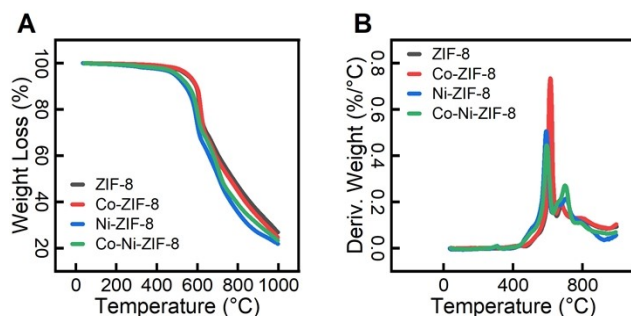


Figure S5. Thermal gravimetric analysis (TGA) of pristine ZIF-8 and metal doped ZIF-8 samples was acquired under N_2 flow at a heating rate of $6\text{ }^\circ\text{C}/\text{min}$.

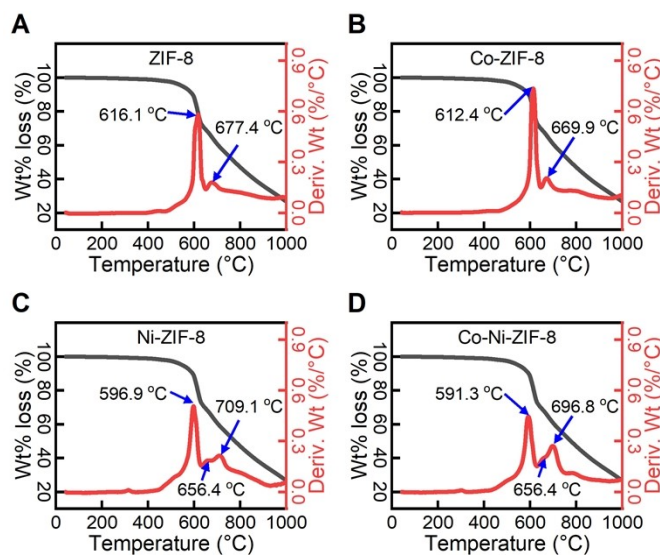


Figure S6. Individual TGA weight loss curves for pristine ZIF-8 and metal doped ZIF-8 samples along with the first derivative of the weight change with respect to temperature. The weigh-loss peak temperature corresponds to the decomposition of framework. Small variations in the peak temperature were observed due to the influence of doped metals.

S6. Inductive Coupled Plasma Optical Emission Spectroscopy

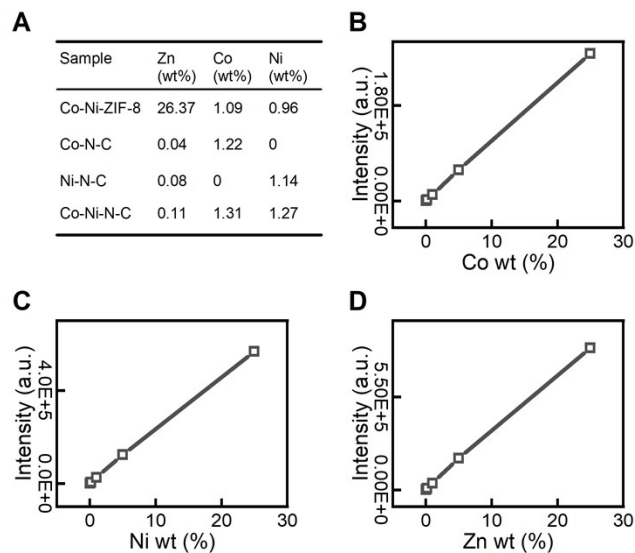


Figure S7. (A) The elemental analysis data of the pristine and carbonized catalysts based on ICP-OES results. (B-D) Calibration plots for (B) Co, (C) Ni, and (D) Zn composition measured using the prepared standards.

S7. Supplementary XPS Spectra

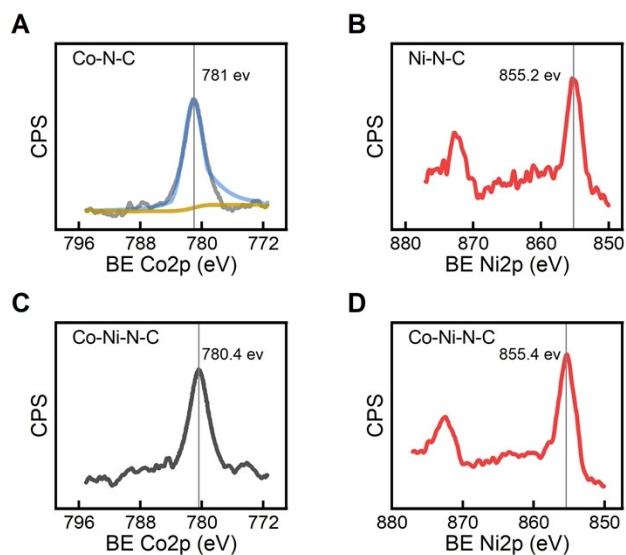


Figure S8. (A) Co 2p XPS spectra of Co-N-C catalyst. (B) Ni 2p XPS spectra of Ni-N-C catalyst. (C) Co 2p XPS spectra of Co-Ni-N-C catalyst. (D) Ni 2p XPS spectra of Co-Ni-N-C catalyst.

S8. Raman Spectroscopy

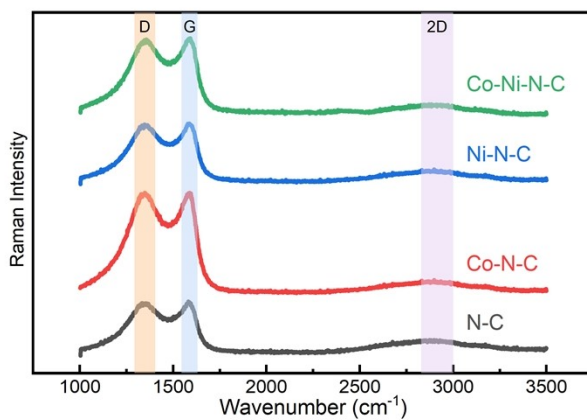


Figure S9. Raman spectra of M-N-C materials. Bands at 1350, 1582, and 2700 cm⁻¹ are assigned to the D, G, and 2D bands of graphitized carbon and the concomitant disorder species.

S9. Diffuse Reflectance Infrared Fourier Transform Spectroscopy

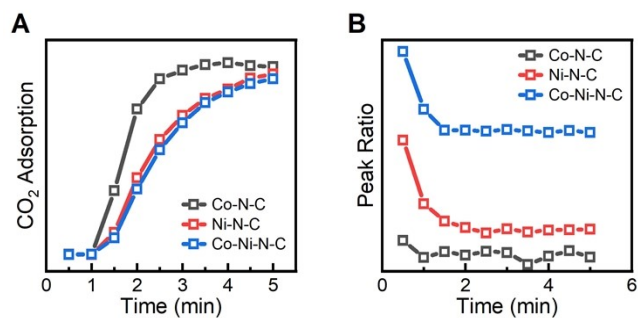


Figure S10. (A) Adsorption kinetics of CO₂. (B) The area ratios of two peaks in the DRIFT spectra as a function of adsorption time.

S10. Temperature-Programmed Analyses

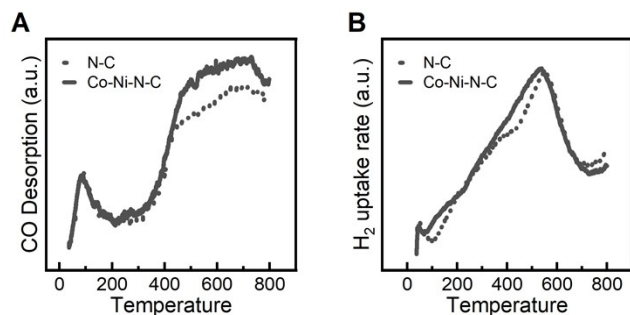


Figure S11. (A) Temperature-programmed desorption (TPD) on N-C and Co-Ni-N-C shows the presence of weaker binding CO sites on Co-Ni-N-C. (B) Temperature-programmed reduction (TPR) on N-C and Co-Ni-N-C shows the absence of reducible metal species.

S11. Additional Electron Microscopy

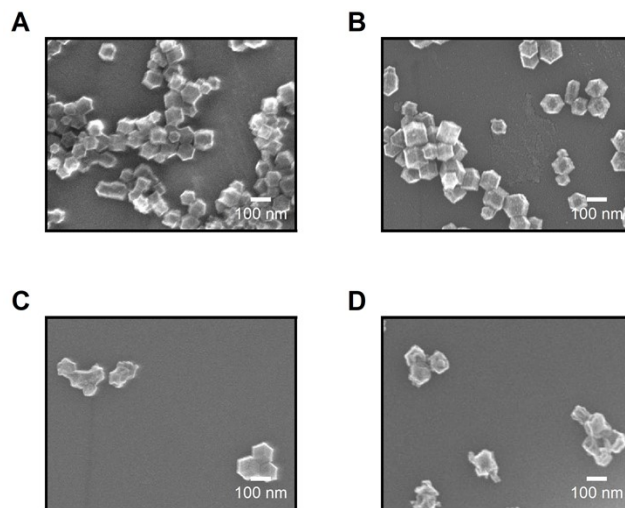


Figure S12. (A-D) Scanning electron microscopy (SEM) images of metal-nitrogen-doped carbons. (A) N-C. (B) Co-N-C. (C) Ni-N-C. (D) Co-Ni-N-C.

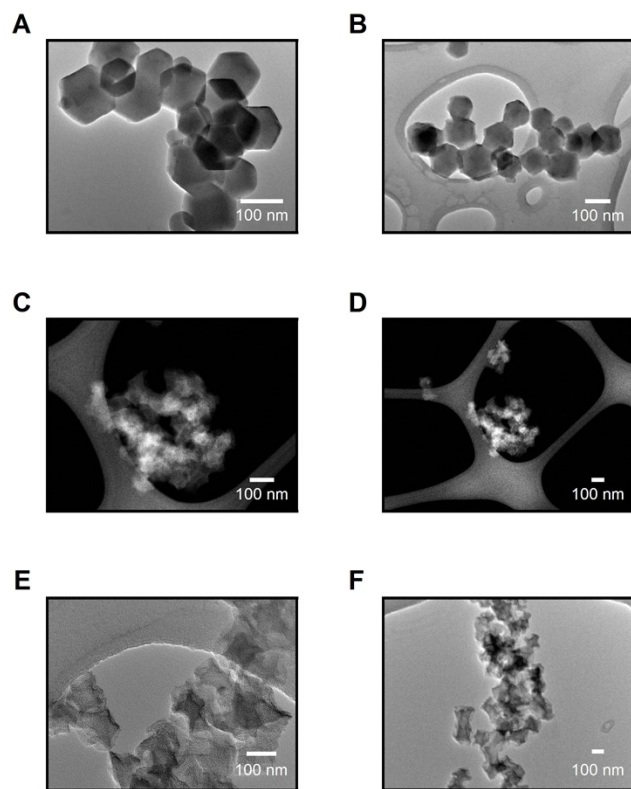


Figure S13. Representative TEM images (**A, B**) of Co-Ni-ZIF-8. HAADF-STEM images (**C, D**) and TEM images (**E, F**) of Co-Ni-N-C.

S12. Linear Sweep Voltammetry

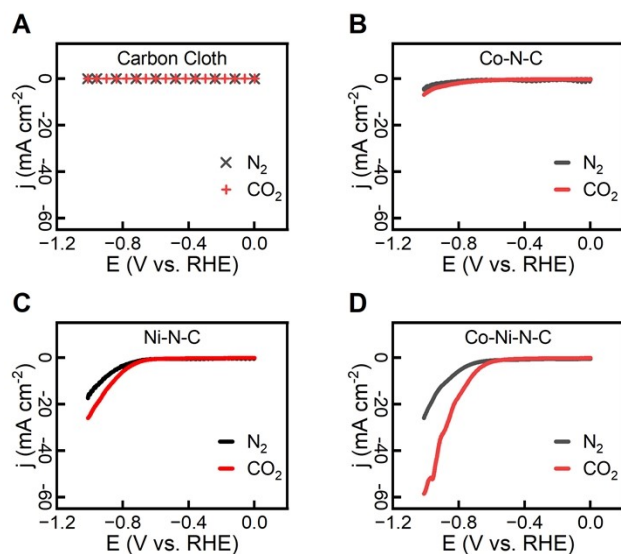


Figure S14. Linear sweep voltammetry performed on four catalysts: (A) N-C, (B) Co-N-C, (C) Ni-N-C, and (D) Co-Ni-N-C. The tests were conducted in CO₂-saturated 0.1 M KHCO₃ (represented by the red line and symbol) and in N₂-saturated 0.1 M KHCO₃ (represented by the black line and symbol).

S13. ¹H Nuclear Magnetic Resonance

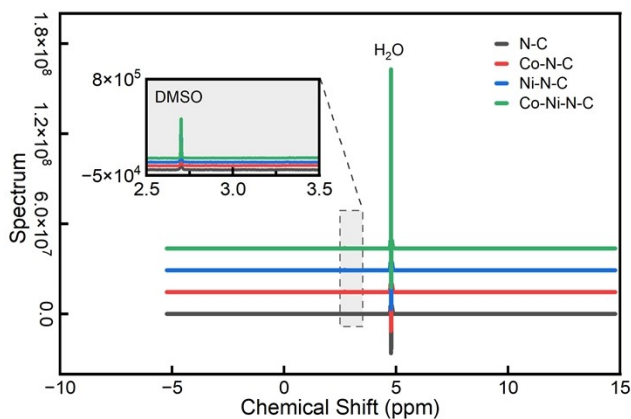


Figure S15. ¹H-NMR spectra of the catholytes with four catalysts at -0.8 V RHE in 0.1 M KHCO₃ after 20 minutes of operation. DMSO was used as an internal standard.

S14. Electrochemically Active Surface Area (ECSA) and Nyquist Plots

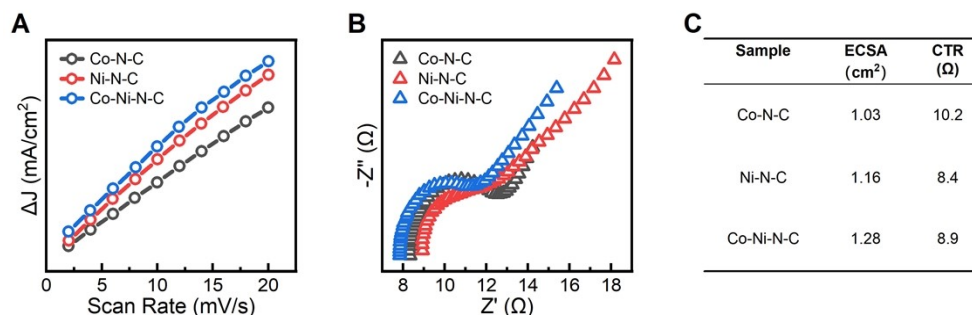


Figure S16. (A) Current as a function of the scan rate of three catalysts obtained from voltammetric scans at different scan rates. (B) Nyquist plots of the three catalysts from 0.1 Hz to 100 kHz in 0.1 M KHCO₃. (C) ECSA values charge transfer resistance (CTR) of the catalysts.

S15. Catalytic Performance Table

Table S1. Selected CO₂ ECR catalysts and their performance in CO₂ reduction.

Materials		Catalytic performance				References
Metal	Support	Product	FE	TOF	Duration	
Co	g-C ₃ N ₄	CO	72%	61.6 h ⁻¹	2 hr	13
Cu	g-C ₃ N ₄	CH ₃ OH	95.5%	—	3 hr	14
Ru	g-C ₃ N ₄	CH ₃ OH	—	—	6 hr	15
In	N-graphene	HCOOH	85.2%	—	12 hr	16
Ni	N-CNT	CO	94%	—	8 hr	17
Ni	N-C nanosheet	CO	100%	—	50 hr	18
Ni	N-graphene	CO	95.6%	1425 h ⁻¹	10 hr	19
Ni	N-graphene	CO	98.4%	17371 h ⁻¹	15 hr	20
Fe, Cu	N-C	CO	95%	5047 h ⁻¹	60 hr	21
Co, Ni	N-C	CO	94.1%	5220 h ⁻¹	40 hr	This work

Note: CNT denotes carbon nanotube. FE signifies faradic efficiency. TOF represents turnover frequency.

S16. Density Functional Theory (DFT) Calculations

Figure S17 shows the model systems for the monatomic and diatomic metal-nitrogen sites. For the monatomic metal nitrogen sites, the metal is coordinated to three nearby nitrogen atoms and one carbon atom, which overall forms a square planar motif as shown in **Figures S17A** and **S17B** for Co-N-C and Ni-N-C, respectively. Meanwhile, in the case of the dual-metal nitrogen sites, each of the metal atoms is coordinated with three nitrogen atoms, while the fourth coordination site lies between the two metals as shown in **Figure S17C**. Geometry optimizations at the RI-PBE0-D3BJ/def2-SVP method reveal that for the Co-N-C complex, the doublet spin state is 0.35 eV more stable than the quartet spin state. For the Ni-N-C complex, the singlet spin state is 0.48 eV more stable than the triplet spin state. In the case of the Co-Ni-N-C complex, the most stable spin state is the doublet state. However, we note that the energies for the other spin states are very close to the doublet state. In particular, the quartet state is only 0.03 eV higher than the doublet state, while the sextet state is only 0.09 eV higher than the double state. In summary, the ground electronic states for the Co-N-C, Ni-N-C, and Co-Ni-N-C complexes are doublet, singlet, and double, respectively.

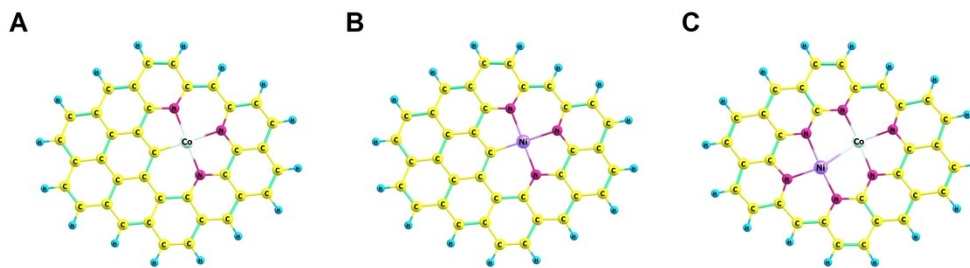


Figure S17. Model systems for assessing the catalytic activities of (A) Co-N-C (B) Ni-N-C, and (C) Co-Ni-N-C.

The CO₂ reduction process was modelled by evaluating the changes in free energy for each of the following processes: Step A: $CO_2 + * + H^+ + e^- \rightarrow COOH^*$. Step B: $COOH^* + H^+ + e^- \rightarrow CO^* + H_2O$. Step C: $CO^* \rightarrow CO + *$. The symbol * denotes the surface, and α^* represents the species α bound to the surface. The computational hydrogen electrode (CHE) model was used for steps A and B.^{22, 23} Recall that in the CHE model, the chemical potential for the $H^+ + e^-$ can be related to the chemical potential of gaseous H_2 and applied potential U .

$$G(H^+) + G(e^-) = \frac{1}{2}G(H_{2(g)}) - eU \quad (S7)$$

Meanwhile, for the other species in steps A to C, geometry minimizations at several spin states were performed at the RI-PBE0-D3BJ/def2-SVP method followed by a frequency calculation to confirm that the structures correspond to a minimum at their respective potential energy surface. The relative energies for the optimized geometries at different spin states are compiled in **Table S2** of the supporting information. The corresponding free energies for each species were obtained at 1 atm and 298.15 K. From here, the free energies for each step are then calculated as follows:

$$\Delta G_{StepA} = G(COOH^*) - G(CO_2) - G(*) - \frac{1}{2}G(H_{2(g)}) + eU \quad (S8)$$

$$\Delta G_{StepB} = G(CO^*) + G(H_2O) - G(COOH^*) - \frac{1}{2}G(H_{2(g)}) + eU \quad (S9)$$

$$\Delta G_{StepC} = G(CO^*) - G(CO) - G(*) \quad (S10)$$

Table S2. Relative energies (eV) between different spin states for the model surface and intermediates in the CO₂ ECR. Geometry optimizations were performed for each spin-state at the RI-PBE0-D3BJ/def2-SVP method.

Structures	Singlet	Doublet	Triplet	Quartet
Co-N-C	N/A	0.000	N/A	0.350
Ni-N-C	0.000	N/A	0.481	N/A
Co-Ni-N-C	N/A	0.000	N/A	0.033
COOH-Co-N-C	0.000	N/A	0.418	N/A
COOH-Ni-N-C	N/A	0.000	N/A	0.848
COOH(Co-Ni-N-C)	0.638	N/A	0.000	N/A
CO-Co-N-C	N/A	0.000	N/A	0.706
CO-Ni-N-C	0.000	N/A	0.458	N/A
CO(Co-Ni-N-C)	N/A	0.088	N/A	0.000

For the bi-metal structure, the reduction of another CO₂ from the *CO intermediate was further investigated. This was done by performing geometry optimizations at the singlet and triplet spin states for the *CO@bridge+*COOH@Ni and *CO@bridge+*COOH@Co intermediates. We found that the triplet spin state is more stable than the singlet spin state for both intermediates.

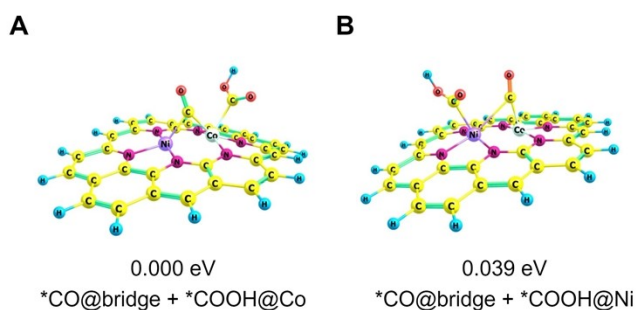


Figure S18. Structures for the *CO@bridge+*COOH@Co and *CO@bridge+*COOH@Ni intermediates and their relative Gibbs free energies.

In addition to DFT studies on the thermodynamics of CO₂ ECR, we have also investigated the HER aspects of the systems presented in this work. We note that in the case of the bi-metallic Co-Ni-N-C surface, there might be several possible adsorption sites for the H atom. As a result, we have searched for structures that have the H adsorbed on the Ni, Co, and bridge of Co and Ni sites. Two stable structures were found from geometry optimizations and are shown in **Figure S19**. These are the H atom adsorbed on the Co atom (**Figure S19A**) and H atom bridged between the Co and Ni atoms (**Figure S19B**). We tried searching for a structure where the H atom is adsorbed on the Ni atom by starting a geometry optimization with a structure that has the H atom biased towards the Ni atom's site. However, geometry optimization revealed that our initial structure would relax to the bridge of Co and Ni structure. The ΔG for the $\text{Surf} + \text{H}^+ + \text{e}^- \rightarrow \text{Surf-H}$ was calculated. It takes 1.88 eV for the H atom to be adsorbed on the Co site. Adsorption of H to yield a bridge structure is more thermodynamically favourable than yielding the Co-H structure because it only requires 1.00 eV to form.

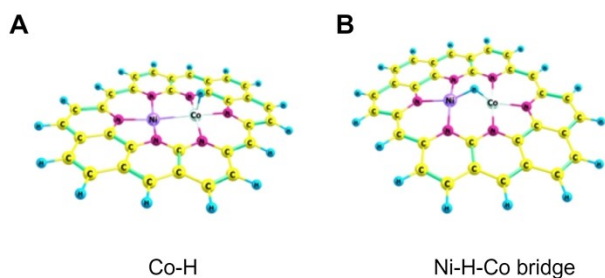


Figure S19. Hydrogen adsorption sites for the HER reaction on the Co-Ni bi-metallic structure.

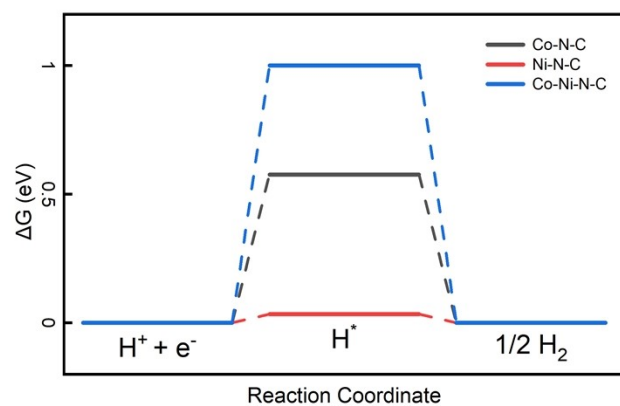


Figure S20. Free energy diagrams for the hydrogen evolution over Ni-N-C, Co-N-C, and Co-Ni-N-C through the H atom bridged between the Co and Ni atoms.

References

1. R. Banerjee, A. Phan, B. Wang, C. Knobler, H. Furukawa, M. O'Keeffe and O. M. Yaghi, *Science*, 2008, **319**, 939-943.
2. Z. Öztürk, M. Filez and B. M. Weckhuysen, *Chemistry – A European Journal*, 2017, **23**, 10915-10924.
3. H. S. Jeon, S. Kunze, F. Scholten and B. Roldan Cuenya, *ACS Catalysis*, 2018, **8**, 531-535.
4. E. L. Clark, J. Resasco, A. Landers, J. Lin, L.-T. Chung, A. Walton, C. Hahn, T. F. Jaramillo and A. T. Bell, *ACS Catalysis*, 2018, **8**, 6560-6570.
5. A. S. Hall, Y. Yoon, A. Wuttig and Y. Surendranath, *Journal of the American Chemical Society*, 2015, **137**, 14834-14837.
6. J. S. Diercks, B. Pribyl-Kranewitter, J. Herranz, P. Chauhan, A. Faisnel and T. J. Schmidt, *Journal of The Electrochemical Society*, 2021, **168**, 064504.
7. T. Chatterjee, E. Boutin and M. Robert, *Dalton Transactions*, 2020, **49**, 4257-4265.
8. D. M. Morales and M. Risch, *Journal of Physics: Energy*, 2021, **3**, 034013.
9. H. Ji, X. Zhao, Z. Qiao, J. Jung, Y. Zhu, Y. Lu, L. L. Zhang, A. H. MacDonald and R. S. Ruoff, *Nature Communications*, 2014, **5**, 3317.
10. S. Anantharaj, P. E. Karthik and S. Noda, *Angewandte Chemie International Edition*, 2021, **60**, 23051-23067.
11. X. Li, X. I. Pereira-Hernández, Y. Chen, J. Xu, J. Zhao, C.-W. Pao, C.-Y. Fang, J. Zeng, Y. Wang, B. C. Gates and J. Liu, *Nature*, 2022, **611**, 284-288.
12. S. Vijay, W. Ju, S. Brückner, S.-C. Tsang, P. Strasser and K. Chan, *Nature Catalysis*, 2021, **4**, 1024-1031.
13. P. Huang, J. Huang, J. Li, L. Zhang, J. He, C. A. Caputo, A. I. Frenkel and G. Li, *ChemNanoMat*, 2021, **7**, 1051-1056.
14. T. Yang, X. Mao, Y. Zhang, X. Wu, L. Wang, M. Chu, C.-W. Pao, S. Yang, Y. Xu and X. Huang, *Nature Communications*, 2021, **12**, 6022.
15. P. Sharma, S. Kumar, O. Tomanec, M. Petr, J. Zhu Chen, J. T. Miller, R. S. Varma, M. B. Gawande and R. Zbořil, *Small*, 2021, **17**, 2006478.
16. D. Xu, Y. Xu, H. Wang and X. Qiu, *Chemical Communications*, 2022, **58**, 3007-3010.
17. Q. Sun, W. Ren, Y. Zhao and C. Zhao, *Chemical Communications*, 2021, **57**, 1514-1517.
18. Y. Zhang, K. Qi, J. Li, B. A. Karamoko, L. Lajaunie, F. Godiard, E. Oliviero, X. Cui, Y. Wang, Y. Zhang, H. Wu, W. Wang and D. Voiry, *ACS Catalysis*, 2021, **11**, 12701-12711.
19. Y. Zhang, L. Jiao, W. Yang, C. Xie and H.-L. Jiang, *Angewandte Chemie International Edition*, 2021, **60**, 7607-7611.
20. C. Lu, K. Jiang, D. Tranca, N. Wang, H. Zhu, F. Rodríguez-Hernández, Z. Chen, C. Yang, F. Zhang, Y. Su, C. Ke, J. Zhang, Y. Han and X. Zhuang, *Journal of Materials Chemistry A*, 2021, **9**, 24955-24962.
21. M. Feng, X. Wu, H. Cheng, Z. Fan, X. Li, F. Cui, S. Fan, Y. Dai, G. Lei and G. He, *Journal of Materials Chemistry A*, 2021, **9**, 23817-23827.
22. A. A. Peterson, F. Abild-Pedersen, F. Studt, J. Rossmeisl and J. K. Nørskov, *Energy & Environmental Science*, 2010, **3**, 1311-1315.

23. J. K. Nørskov, J. Rossmeisl, A. Logadottir, L. Lindqvist, J. R. Kitchin, T. Bligaard and H. Jónsson, *The Journal of Physical Chemistry B*, 2004, **108**, 17886-17892.